Earth and Space Science

RESEARCH ARTICLE
10.1029/2019EA000695

Shallow Seafloor Gas emissions Near Heard and McDonald Islands on the Kerguelen Plateau, Southern Indian Ocean

E. A. Spain[1], S. C. Johnson[1,2], B. Hutton[3], J. M. Whittaker[1], V. Lucieer[1], S. J. Watson[1,4], J. M. Fox[1,5], J. Lupton[6], R. Arculus[7], A. Bradney[7], and M. F. Coffin[1,8,9]

[1]Institute for Marine and Antarctic Studies, University of Tasmania, Hobart, Tasmania, Australia, [2]Irish Centre for Research in Applied Geosciences (iCRAG), University College Dublin, Dublin, Ireland, [3]Echoview Software Pty. Ltd., Hobart, Tasmania, Australia, [4]Coasts and Oceans, National Institute for Water and Atmospheric Research, Auckland, New Zealand, [5]Centre for Ore Deposit and Earth Sciences, University of Tasmania, Hobart, Tasmania, Australia, [6]National Oceanic and Atmospheric Administration, Pacific Marine Environmental Laboratory, Newport, OR, USA, [7]School of Earth Sciences, Australian National University, Canberra, Australian Capital Territory, Australia, [8]School of Earth and Climate Sciences, University of Maine, Orono, ME, USA, [9]Geology and Geophysics, Woods Hole Oceanographic Institution, Woods Hole, MA, USA

Key Points:
- Active submarine gas emission around Heard and McDonald Islands on the Central Kerguelen Plateau in the southern Indian Ocean
- Gas release near the McDonald Islands possibly shallow diffuse hydrothermal venting, uncommon on an intraplate large igneous province
- Gas release near Heard Island either or both a biogenic orthermogenic methane seep, the second reported in the Southern Ocean to date

Supporting Information:
- Supporting Information S1
- Figure S1
- Figure S2
- Table S1
- Table S2
- Table S3

Correspondence to:
E. A. Spain,
erica.spain@utas.edu.au

Citation:
Spain, E. A., Johnson, S. C., Hutton, B., Whittaker, J. M., Lucieer, V., Watson, S. J., et al. (2020). Shallow seafloor gas emissions near Heard and McDonald Islands on the Kerguelen Plateau, Southern Indian Ocean. *Earth and Space Science*, *7*, e2019EA000695. https://doi.org/10.1029/2019EA000695

Received 29 APR 2019
Accepted 9 SEP 2019
Accepted article online 10 DEC 2019

Abstract Bubble emission mechanisms from submerged large igneous provinces remains enigmatic. The Kerguelen Plateau, a large igneous province in the southern Indian Ocean, has a long sustained history of active volcanism and glacial/interglacial cycles of sedimentation, both of which may cause seafloor bubble production. We present the results of hydroacoustic flare observations around the underexplored volcanically active Heard Island and McDonald Islands on the Central Kerguelen Plateau. Flares were observed with a split-beam echosounder and characterized using multifrequency decibel differencing. Deep-tow camera footage, water properties, water column δ^3He, subbottom profile, and sediment δ^{13}C and δ^{34}S data were analyzed to consider flare mechanisms. Excess δ^3He near McDonald Islands seeps, indicating mantle-derived input, suggests proximal hydrothermal activity; McDonald Islands flares may thus indicate CO_2, methane, and other minor gas bubbles associated with shallow diffuse hydrothermal venting. The Heard Island seep environment, with subbottom acoustic blanking in thick sediment, muted ^{3}He signal, and δ^{13}C and δ^{34}S fractionation factors, suggest that Heard Island seeps may either be methane gas (possibly both shallow biogenic methane and deeper-sourced thermogenic methane related to geothermal heat from onshore volcanism) or a combination of methane and CO_2, such as seen in sediment-hosted geothermal systems. These data provide the first evidence of submarine gas escape on the Central Kerguelen Plateau and expand our understanding of seafloor processes and carbon cycling in the data-poor southern Indian Ocean. Extensive sedimentation of the Kerguelen Plateau and additional zones of submarine volcanic activity mean additional seeps or vents may lie outside the small survey area proximal to the islands.

Plain Language Summary Bubbles are constantly escaping the seafloor, either from thick sediments with gas-producing bacteria or from volcanic gases escaping rocks deep beneath the seafloor. We use sonar to observe bubbles that appear as "hydroacoustic flares" as they travel from the seafloor into the ocean. Our paper shows the results of the 2016 RV *Investigator* voyage to Heard and McDonald Islands, two of Australia's most remote islands and home to its only active volcanoes. We observed hundreds of flares around the two islands and were able to examine bubbles in some of our camera footage. By examining the seafloor, the shallow subseafloor, and the chemistry of sediments and the water column, we suggest the bubbles may be composed of different gases. Around Heard Island, bubbles were associated with thick sediment that are likely rich with bacteria that produce methane gas; near the McDonald Islands, bubbles were not associated with sediments and possibly indicate shallow volcanic activity emitting gases, like CO_2, originating from the mantle. Knowing where bubbles are escaping is crucial for understanding how much gas is contributed from the seafloor into the ocean and atmosphere.

1. Introduction

Bubble emission from the seafloor abounds in the global ocean. Predominantly hydrocarbon or hydrothermal in nature, gas seeps and vents are found in diverse geological settings and can aid our understanding of

the deep-Earth and shallow seafloor processes (De Beukelaer et al., 2003; Gentz et al., 2014; Hovland et al., 2012; Murton et al., 1994; Nakamura et al., 2015; Passaro et al., 2016; Pérez et al., 2014; Riedel et al., 2001; Rona et al., 1991; Rona et al., 2002; Weber et al., 2014). Submarine gas emissions manifest as water column hydroacoustic "flares" in shipboard echosounders as the impedance contrast bubbles create with the surrounding seawater makes them excellent acoustic scatterers (Clift et al., 1978; Colbo et al., 2014; McCartney & Bary, 1965; McGinnis et al., 2006).

The primary source of hydroacoustic flares is methane bubbles from cold methane seeps that are widespread on active and passive margins, where organic-rich sediment readily accumulates (Judd, 2003; Kirschke et al., 2013; Reeburgh, 2007; Suess, 2014). Methane seeps are the seafloor expression of the following: (1) methanogenesis, the microbial decomposition of organic matter in anoxic sediments; (2) thermogenesis, the thermo-catalytic breakdown of deep buried organic matter; or (3) dissolution of methane hydrates, which are stable in low-temperature, high-pressure settings but dissociate above the gas hydrate stability zone (GHSZ).

Gas emissions adjacent to hydrothermal fluid venting can also produce hydroacoustic flares (Hernández et al., 2017; Passaro et al., 2014; Passaro et al., 2016; Pérez et al., 2012). A majority CO_2, abiotic methane, and other minor gas bubbles or CO_2 liquid droplets are commonly attributed to localized degassing along regional fracture systems from deeper mantle sources (Passaro et al., 2014). Only high-frequency or close-range hydroacoustic systems would be able to identify fluid density changes caused by hot hydrothermal fluid venting or freshwater inputs from submarine groundwater discharge (Colbo et al., 2014; Crawford & Hay, 1993; Hay, 1984; Judd & Hovland, 2009) as these signals are typically more subtle as the impedance contrast is lower.

Gas escape along continental margins is well understood (Hovland et al., 2012; Judd, 2003), yet in many remote and/or undersampled locations, seafloor gas emissions are both poorly mapped and poorly constrained. Heard Island and McDonald Islands (HIMI) are a sub-Antarctic island group in the southern Indian Ocean (Figures 1a and 1b). HIMI, along with the Kerguelen Islands, are the currently subaerial portions of the Kerguelen Plateau, a predominantly cretaceous large igneous province (LIP) attributed to the Kerguelen hotspot or mantle plume (Coffin & Eldholm, 1994; Coffin et al., 2002; Figure 1a). HIMI have been constructed on the ~100 Myr Central Kerguelen Plateau and are both active hotspot volcanoes, forming since <1 Ma (Duncan et al., 2016) and <100 Ka (Quilty & Wheller, 2000), respectively (Figure 1b). Both island groups are volcanically active, making submarine extensions of subaerial geothermal systems probable. The current phase of volcanism began at ~400 to 200 Ka, with activity both pre- and post-dating the last glacial maximum (LGM) when a large ice cap covered the two islands (Hodgson et al., 2014; Duncan et al., 2016; Figure 1b). Around 70% of Heard Island's landmass remains obscured by glaciers. Glacial erosion dominates Heard Island and provides a constant source of glaciogenic material to the adjacent seafloor. Extensive submarine volcanism between 59 Ma and 21 Ka, with numerous examples <1 Ma, has also been documented across the broader Central Kerguelen Plateau (Weis et al., 2002).

We report the first scientific hydroacoustic, geochemical, geophysical, and video data from the water column, seafloor, and subseafloor surrounding HIMI, collected during the IN2016_V01 voyage of Australia's Marine National Facility RV *Investigator* where 13 gas seeps were observed around the islands in water depths of <200 m. In the absence of direct gas samples from these remote seeps, we analyze and interpret hydroacoustic flare observations, combined with water column δ^3He, sediment δ^{13}C and δ^{34}S, deep-tow camera footage, conductivity-temperature-depth (CTD), and subbottom profile data to understand the distribution of seeps and consider the origin and implications of the gas emissions.

2. Materials and Methods

2.1. Hydroacoustic and Subbottom Profile

A Simrad EK60 multifrequency split-beam echosounder recorded water column data at ship speeds ≤10 knots. We analyzed EK60 data collected at 38 and 120 kHz frequencies, both with a beam width of 7°. Pulse length was 2.048 ms^1 for 38 kHz and 1.024 ms^1 for 120 kHz. A sound velocity of 1513.78 ms^1 was applied to all EK60 data. The echosounder was calibrated prior to the voyage using the standard target method with a 20-mm tungsten-carbide sphere (Foote et al., 1987). For cogency, the term "acoustic

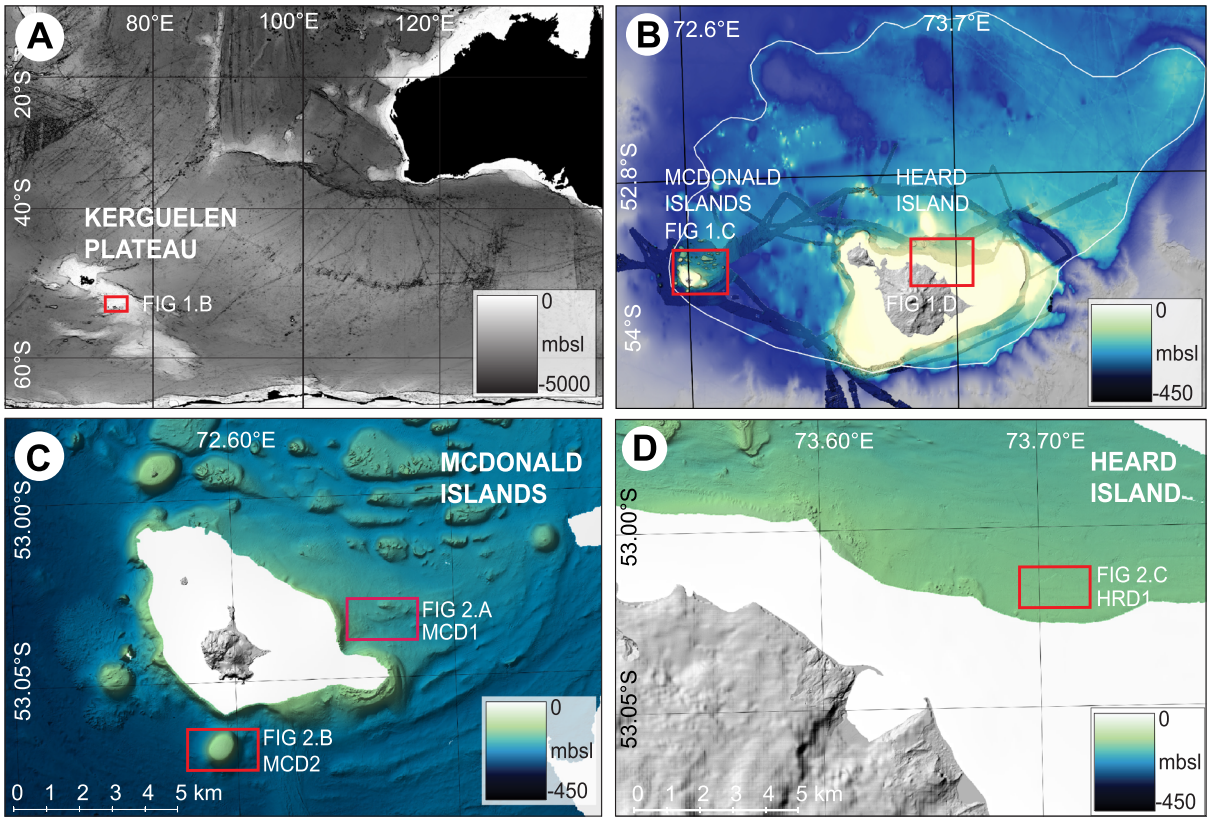

Figure 1. Maps of (a) the Kerguelen Plateau (30 arc-sec bathymetry GEBCO_2014); (b) Central Kerguelen Plateau, with Heard Island and McDonald Islands (HIMI) showing paleo-ice sheet margin (white line; 100-m bathymetry (Beaman & O'Brien, 2011)); (c) McDonald Islands study sites (MCD1 and MCD2); (d) Heard Island study site (HRD1). (c) and (d) 10-m bathymetry from IN2016_V01 EM710 multibeam echosounder.

anomalies" will herein describe clusters of higher-intensity water column backscatter that cover multiple pings in the time dimension and multiple samples in the depth dimension; the term "flare," "hydroacoustic flare," or "flare observation" describes individual acoustic anomalies that characterize free gas bubble emission from the seafloor; and the term "seep" describes locations where individual flares were surveyed multiple times over repeat survey passes and thus grouped together as a seep.

Acoustic anomalies were identified in the EK60 echograms, analyzed, and characterized using a processing methodology applied in the Echoview software package (Version 7.0.90; Text S1). Acoustic anomalies attributable to fish schools, large biological scatterers (such as diving penguins and seals), seafloor reflections, and interference from other hydroacoustic systems were manually removed, as were incomplete observations due to data gaps. The remaining anomalies were considered flare observations if they were rooted to the seafloor and detected at least twice in the same approximate location during subsequent passes, following Gentz et al. (2014) and Veloso et al. (2015). Flare locations were georeferenced in Echoview by the GPS location of the middle ping of each flare in the split-beam data. Due to the spatial uncertainty associated with the location in the beam for aggregated backscatter in split-beam echosounder data, flares were not defined as individual flares but grouped as seeps for written clarity.

Flares were classified using a customized multifrequency decibel differencing technique (Figures S1.f–S1.i). Decibel differencing compares water column backscatter across two synchronized frequencies using a calibrated echosounder. Due to the nature of acoustic pressure waves, backscatter recorded for different frequencies varies depending on bubble or target properties. Frequency differences can be exploited to classify biological water column scatterers due to the presence of a swim bladder (Brierley & Watkins, 1996; Madureira et al., 1993), and we applied the technique here to water column gas bubbles. A mean volume backscatter strength (ratio of 120–38 kHz or ΔMVBS; acoustic intensity in decibels) frequency

response filter of −20 to 1 dB was created using the acoustic response of the flares, where bubbles were observed in camera footage (see section 2.2). The frequency response filter was then applied to all echograms, where no bubbles were visible in the limited camera footage or for which no footage was collected, to classify the remaining flares (Figures 1.h and 1.i).

A Kongsberg SBP120 subbottom profiler, using linear chirp at 2 to 8 kHz, operated synchronously with the EK60. Raw SBP120 data were imported as SEG-Y files into the Fledermaus FM Midwater software package (Version 7.7.4) for visualization. Files were merged with navigation data and converted to generic water column format. We interpreted sedimentary structures in the subbottom profiles, focusing on sedimentary horizons and acoustic blank zones beneath flares.

2.2. Water Column and Seafloor Observations

A high-definition deep-tow camera system was deployed nine times over the three sites (Figures 1c and 1d) where we observed strong persistent flares (Figures 2a–2c). The deep-tow camera system houses a Canon EOS-1DX still/video camera (34° angle of view; focal length = 70–200 mm; aperture = min f/2.8, max f/32; minimum focus distance = 1.5 m; exposure = 1/125) and a Canon C300 HD cinema video camera (~50° viewing angle). The Canon EOS-1DX was the primary system for both video and still camera footage. Track lengths and mean altitude values were calculated when the camera was within 10 m of seafloor. Visibility distance was estimated when the seafloor ceased being visible in the video footage (Table S1).

The deep-tow video and camera footage were examined to identify visible bubble streams or evidence of seafloor emissions, and thousands of high-resolution still images were examined for seafloor structures and benthic habitats. Bubbles sizes were determined by comparing their sizes at the seafloor with the camera laser sights (10 cm apart at the seafloor). Observed bubbles were georeferenced using the dedicated ultrashort baseline of the camera system.

The deep-tow camera system has a comounted SBE 37-SI MicroCAT CTD, located ~0.75 m aft of the camera system. CTD data were analyzed for any temperature/salinity anomalies present near flares. Sampling frequency of the CTD was 1.5 s, with an instrument resolution of 0.0001 mS/cm for conductivity, ± 0.0001 °C for temperature, and 0.002% of full-scale range for pressure.

2.3. Helium Samples

We used helium isotopes from water samples to differentiate flares potentially related to hydrothermal activity. Hydrothermal fluids are enriched in light helium, ^{3}He, relative to atmospheric helium, ^{4}He, as their source is the mantle. The mantle is enriched in ^{3}He making $^{3}He/^{4}He$ isotope ratios, therefore, useful indicators for mantle input into the ocean. Volcanic rocks of Heard Island have high $^{3}He/^{4}He$ ratios, up to 18 times the atmospheric ratio due to the involvement of a deep-seated mantle plume during its evolution (Hilton et al., 1995). Any hydrothermal input from the flanks of HIMI would therefore be expected to have comparably elevated ^{3}He; flares unrelated to hydrothermal activity (i.e., cold methane seeps) are expected to contain radiogenic helium with a lower $^{3}He/^{4}He$ ratio.

During the voyage, 74 seawater samples were immediately drawn from Niskin bottles on the shipboard CTD rosette and hermetically sealed into copper tubes using a hydraulic crimping system (Young & Lupton, 1983). Samples were analyzed onshore for ^{3}He and ^{4}He concentrations and $^{3}He/^{4}He$ ratios by mass spectrometry. Approximately half of the samples were reference samples collected in four vertical profiles spanning the Kerguelen Plateau north of HIMI to establish regional background $^{3}He/^{4}He$ levels (Figure 2d) and search for the presence of a ^{3}He plume emanating from HIMI (Table S2). In addition to the Kerguelen Plateau profiles, another 32 samples were collected during shallow casts in the vicinity of flares with samples collected near the bottom of each CTD cast. The $^{3}He/^{4}He$ is reported in units of $\delta^{3}He$ (%), which is the percentage deviation from atmospheric $^{3}He/^{4}He$.

2.4. Sediment Samples

Two sediment samples from a Smith-McIntyre grab (SMG) suitable for geochemical analyses were recovered from near HRD1.2 seep (SMG-03 and SMG-08; Figure 2c). No samples proximal to MCD1 seeps were viable for geochemical analyses as they were composed of pumice and sand. No samples were collected near MCD2 due to hard seafloor. Samples were split, freeze-dried, and sieved to separate the sediment from biogenic material (i.e., shell fragments). Weight % of bulk carbonate ($^{13}C_{carb}$) and ^{34}S were determined using an

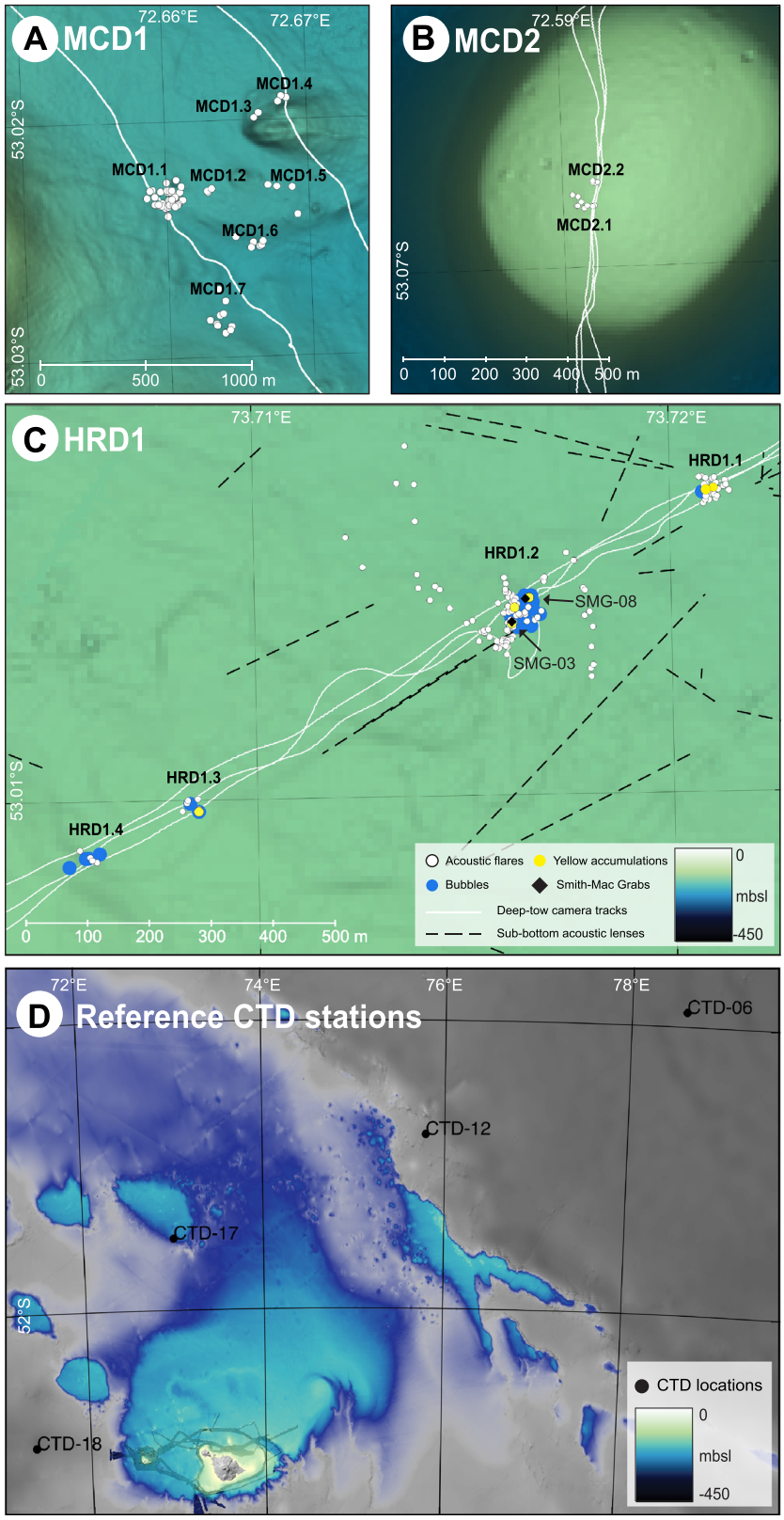

Figure 2. Sample locations (a) MCD1, (b) MCD2, and (c) HRD1, with observed flares, bubbles, yellow matter, and SMG sample sites. (d) Map of four CTD casts analyzed for background helium isotopes spanning the Kerguelen Plateau north of HIMI. Color bar applies to all maps.

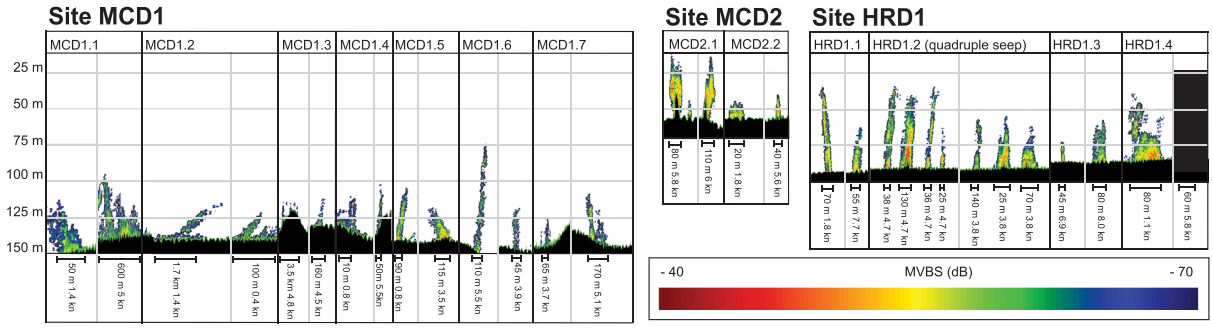

Figure 3. Compilation of flares observed at the three sites (MCD1, MCD2, and HRD1). Vertical axis is water depth, 25 m intervals; horizontal axis is calculated from time (UTC) and average ship speed. Top 10 m of water and all data below the seafloor are removed (black areas). Flares are colored by mean volume backscatter strength (MVBS; acoustic intensity, dB), red the highest (–40 dB), and blue the lowest (–70 dB). All flares have been cleaned, threshold filtered, and resampled in Echoview.

Eltra CS-2000 elemental analyzer (Durand et al., 2017; Johnson et al., 2017). Each powdered sample was combusted at >1,500 °C in pure (99.99%) oxygen, causing carbon to form carbon dioxide (CO_2) and sulfur to react to sulfur dioxide (SO_2); reactions were measured on four infrared (IR) channels. The machine was calibrated to Eltra supplied standards, international standards (AR-4007, AR-4019, AR-4015, and Choice Analytical), and internal standard (QLDSED). Data accuracy and reproducibility are better than 0.02% for S and 0.05% for C. Weight % of bulk organic carbon ($^{13}C_{org}$) was determined using the same method; however, the samples (~500 mg) were pretreated using an acid treatment of 6 N HCl on a hotplate at 70 °C for 8 hr to promote dissolution of inorganic carbon species. The samples were rinsed with distilled water and dried overnight, and the dried residue was analyzed using the aforementioned method.

Duplicate samples were sieved, powdered, and analyzed for carbon and sulfur isotopes at the Central Science Laboratory, University of Tasmania. The $\delta^{13}C_{carb}$ component was derived by treating the powders with phosphoric acid (100% H_3PO_4, 50 °C, 24 hr). The evolved CO_2 was purified by means of subsequent cold traps ($N_{2\ (liq.)}$ −196 °C and acetone/CO_2 −94 °C) to remove noncondensable reaction by-products and analyzed using a dual-inlet VG-Optima. The $\delta^{13}C_{org}$ component was derived using the same method as outlined for C_{org}% to evolve inorganic carbon species and analyzed using an Isoprime 100 PyroCube. Some samples (organic-rich sediments) yielded little CO_2 and could not be analyzed. Sulfur isotope ($\delta^{34}S$) analysis was conducted also using the Isoprime 100 PyroCube. Analytical uncertainty is less than 0.05‰; reproducibility based on full duplicate analyses and internal and international standards was better than 0.3‰ for all analyses

3. Results

3.1. Flare Identification and Classification

We identified 13 distinct seeps at 3 sites (composed of >200 individual hydroacoustic flare observations; Figures 1c and 1d) originating from the seafloor in water depths of 55–150 m (Figure 3): 7 seeps at MCD1 site (Figure 2a), 2 seeps at MCD2 site (Fig. 2b), and 4 seeps at HRD1 site (Figure 2c). All flare observations are listed in Supporting Information Table S3 with each seep composed of multiple flare observations.

The seven seeps at MCD1 occur on sloping seafloor northeast of the McDonald Islands (mean water depth ~130 m; Figure 2a). Many MCD1 seeps were not persistent during multiple passes nor maintained a consistent morphology (Figure 3). Some flares were observed to be ellipsoid shaped, sometimes slanting; other flares were observed as weak, diffuse scattering near the seafloor (Figure 3; Table S3). MCD1 flares averaged 28 m in height from the seafloor, with a maximum height of 74 m (Figure 3).

The two seeps at MCD2 occur on top of a shallow sea knoll south of the McDonald Islands (mean water depths ~60 m; Figure 2b). Seeps were persistent in the water column during multiple survey passes, with vertically elongated ellipsoid shapes. MCD2 flares averaged 31 m in height from the seafloor, with a maximum height of 48 m; the tallest flares were within 15 m of the sea surface (Figure 3; Table S3).

The four seeps at HRD1 occur on flat seafloor northeast of Heard Island (mean water depths ~90 m; Figure 2c). Seeps were persistent in the water column over multiple survey passes, with tall vertically elongated shapes. HRD1 flares averaged 33 m in height from the seafloor, with a maximum height of 79 m (Figure 3); the tallest flares were within 15 m of the sea surface (Figure 3; Table S3). The flares of HRD1.2 seep (a tight cluster of four discrete flares) were repeatedly observed; however, due to the spatial uncertainty associated with each flare's origin in the split-beam echosounder beam, we grouped them as one seep for clarity.

3.2. Flare Classification

All HRD1 flares were classified by the ΔMVBS filter of −20 to 1 dB. The broad decibel range reflects a broad distribution of bubble sizes. A higher-intensity response in the lower 38 kHz echogram (Figure S1.h) is consistent with gas-filled resonant sphere models, where the relative frequency response peaks in lower frequencies (18 or 38 kHz) and diminishes in higher frequencies (Brierley & Watkins, 1996; Everson et al., 1993; Madureira et al., 1993). HRD1 flare intensity varied little during multiple passes, allowing the filter to work consistently, suggesting continuous seep activity. All MCD2 flares were also captured by the HRD1 ΔMVBS filter of −20 to 1 dB, confirming the flares are caused by gas emission from the seafloor with a similar broad distribution of bubble sizes to HRD1 flares, with a higher-intensity response in the lower 38 kHz frequency. The flares did not have varied intensity during multiple passes, suggesting continuous activity.

Few MCD1 flares were captured by the HRD1 ΔMVBS filter of −20 to 1 dB (Figure S1.h). More MCD1 flares were captured using a second frequency response filter (ΔMVBS = 1 to 20 dB; Figure S1.i), demonstrating a dominant response in the higher 120 kHz echogram, though flares varied in intensity over multiple survey passes. As MCD1 flares were captured in both the HRD1 video-verified ΔMVBS classification (−20 to 1 dB) and the nonverified ΔMVBS classification (1 to 20 dB), a much broader bubble size distribution than both HRD1 and MCD2 is expected though dominant target sizes are smaller than HRD1 and MCD2.

3.3. Subbottom Profile Assessment

At MCD1 (Figure 4a), the subbottom data reveal a strong seafloor and subseafloor reflection of varying relief (Figure 4d). A thin (~5 m) layer of sediment accumulation is observed beneath two seep locations, MCD1.5 and MCD1.6 (Figure 4a), with the acoustic signal obscured below. No distinct horizons or acoustically transparent lenses were imaged. At MCD2 (Figure 4b), the subbottom data reveal a strong seafloor reflection, associated with the shallow sea knoll (Figure 4e). The sea knoll has gentle relief on its summit and steep relief on its flanks. No sediment accumulation was imaged at MCD2.

At HRD1 (Figure 4c), the subbottom data reveal gentle seafloor relief, with continuous reflections delineating stratigraphic units beneath the seafloor to depths of ~20 m (Figures 4f and 4g), with alternating strong and weak reflections. Subsurface acoustically transparent lenses were imaged both beneath observed flares (Figures 4f and 4g) and in the vicinity of and to the northeast of HRD1 without any observed coincident water column flares (Figure 4c). Most acoustic lenses sit beneath the same undulating horizon marked by a strong reflection that sits a few meters below the seafloor (Figures 4f and 4g). Acoustic blanking of the signal occurs beneath these lenses and beneath a strong acoustic reflector, with the signal lost ~20 m beneath the seafloor.

3.4. Water Column and Seafloor Assessments

3.4.1. Temperature and Salinity

CTD measurements collected coincidently with the towed camera did not record any near-seafloor temperature or salinity perturbations at any sites where towed camera footage was collected (Figure S2). No water column stratification was observed, indicating a mixed layer from sea surface to seafloor (Holmes et al., 2019). The near-seafloor water around HRD1 was ~0.3 °C warmer than both MCD1 and MCD2, likely due to its shallower depths. Salinity showed regional variation, with a lower median of 33.87 PSU for HRD1, compared to 33.91 PSU for both MCD1 and MCD2 (Figure S2). The CTD was located ~0.5 above and ~0.75 m aft of the camera, with a mean altitude range of 2.5 and 4.0 m.

3.4.2. Seafloor Camera Observations

Gas bubbles were observed originating from the seafloor at HRD1 (Figure 5), coinciding with all four seeps (Figure 2c). Variations in estimated bubble diameters (~5 to 15 mm) coincide with the broad size distribution

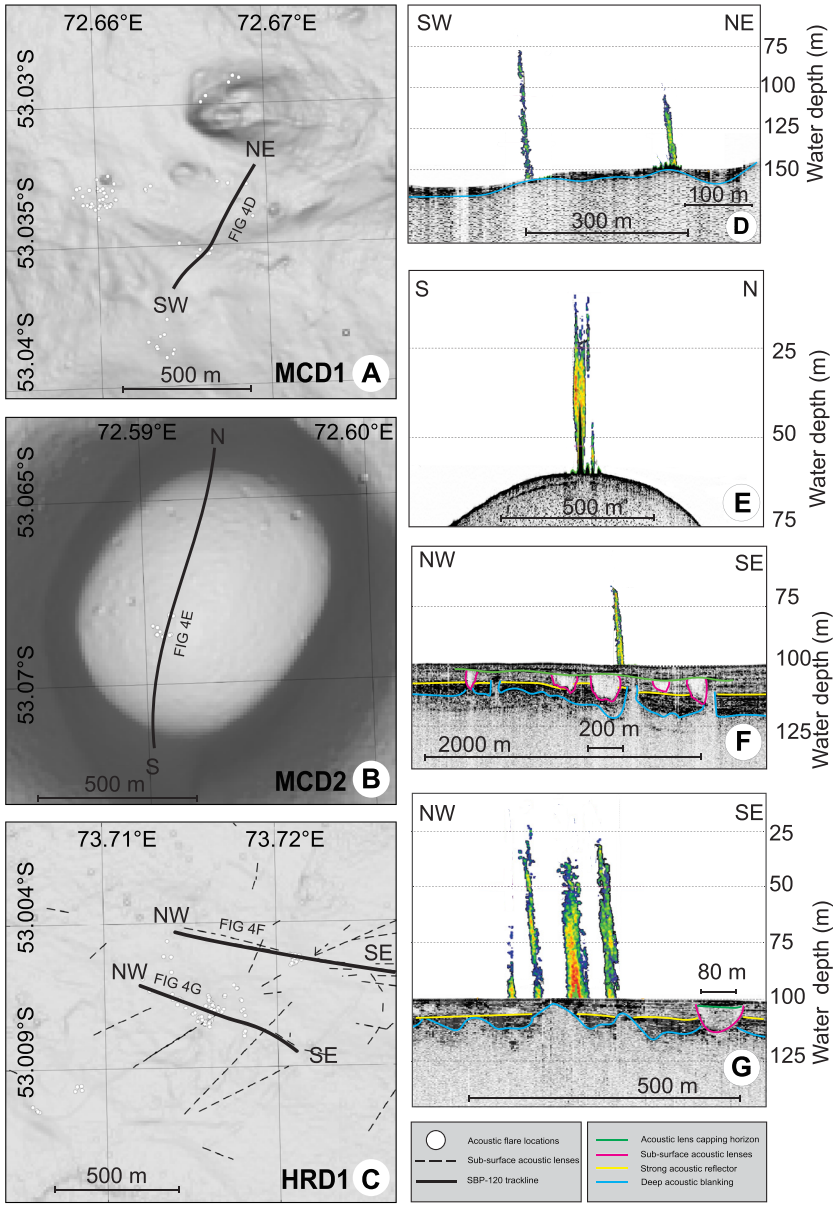

Figure 4. Plan view of three subbottom profile lines at (a)MCD1, (b) MCD2, and (c) HRD1. Subbottom shown in (d) MCD1, (e) MCD2, and (f and g) HRD1, with EK60 flares overlain. Vertical axis is depth, calculated from two-way travel time (assuming constant sound speed of 1500 m/s applied to the SBP120).

expected from the ΔMVBS classification. Bubble sizes were consistent with those observed at other global seeps (~4 to 20 mm; Greinert & Nützel, 2004). Bubble flow rates varied visibly from fast-flowing small bubble streams (Figures 5a–5f) to slow-rising, larger bubbles of an oblate wobbly character (Figure 5c and 5d).

HRD1.1, HRD1.2, and HRD1.3 seeps (Figures 5a–5d) host patchy accumulations of dense yellow matter of varying morphology from a ~5-cm diameter ring (Figure 5b) to an elongated ~40-cm feature (Figure 5d). Most observable bubble streams originate from the yellow matter, with three bubble streams expressed from distinct ~2-cm diameter openings (Figures 5a–5d). Some bubbles observed near HRD1.2 and the observable bubble streams of HRD1.4 (Figure 5f) exit the seafloor from sediment with no associated yellow matter. The seafloor surrounding HRD1 seeps is composed of unconsolidated sediment and coral rubble (Figures 6a–6e) with a variety of epibenthic invertebrates, primarily echinoderms (feather stars, Figures 6a and 6e; sun stars,

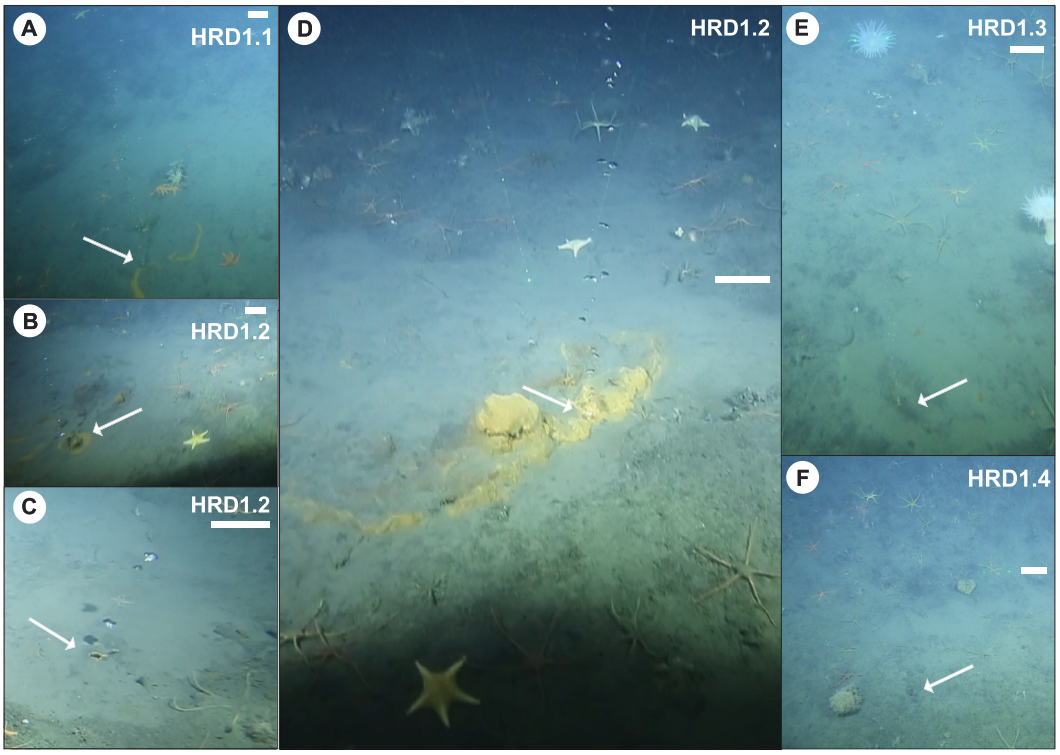

Figure 5. Photographs from HRD1(a) and (b) have consistent bubble streams; (c) a small seep, with larger (~1.5 cm) wobbly, oblate bubbles; (d) the largest extent of yellow accumulations, ~40-cm long; (e) and (f) are thinner streams, with no obvious yellow matter. White scale bars are 10-cm long at the seafloor. Camera tows and observed bubble locations are shown in Figure 2.

Figure 6b; brittle stars, Figures 6c and 6d; sea stars, Figures 6d and 6e; and basket stars), along with fish, crinoids, rays, and skates (not shown). A patch of relict tubeworms was also observed (Figure 6c).

No bubbles were observed in footage from any MCD1 camera deployments (these covered MCD1.1 and MCD1.7 seeps) although visibility was poor due to the turbid water column (estimated to be <2 m). Any bubbles present would likely be indistinguishable from water column particulate matter. The seafloor at MCD1.1 seep is covered in extensive ripples (Figures 6f and 6g). Large (>1-m long, ~1-m wide) defined trenches in the surficial sediment are bare and contain no ripples (Figures 6f and 6g). MCD1.1 hosts echinoderms, though scarcer and less diverse than at HRD1, with yellow brittle stars the dominant visible seafloor biota (Figures 6f and 6g). The seafloor at MCD1.4 was more difficult to observe due to a higher camera altitude; however large boulders, anemones, and ripples were present (Figures 6h and 6i). The flares were located on the flanks of a seafloor mound, with seep locations barren within disturbed sediment patches. No yellow material was observed at either site or any obvious location of bubble release.

No bubbles, ripples, seafloor matter, or visible biota were observed at MCD2 site, although visibility was extremely poor due to the turbid water column (estimated to be <2 m). The seafloor at MCD2 site consists of cream to light gray coarse-grained sediment demarcated by prominent lines of darker, fine-grained sediment (Figures 6j–6m). The lines correspond to flare locations and consist of centimeter-wide central channels; some infilled with white material, with ~10-cm-wide fine-grained darker material berms on either side (Figures 6j–6m).

3.5. Helium Analyses

Background helium profiles taken across the Kerguelen Plateau (Figure 2d) increase smoothly to δ^3He values of ~9% at depths greater than 1000 m (Figure 7a), consistent with previous measurements of ^{3}He/^{4}He in the southern Indian Ocean (Hilton et al., 1995), thereby showing no evidence for local input from HIMI in the reference samples.

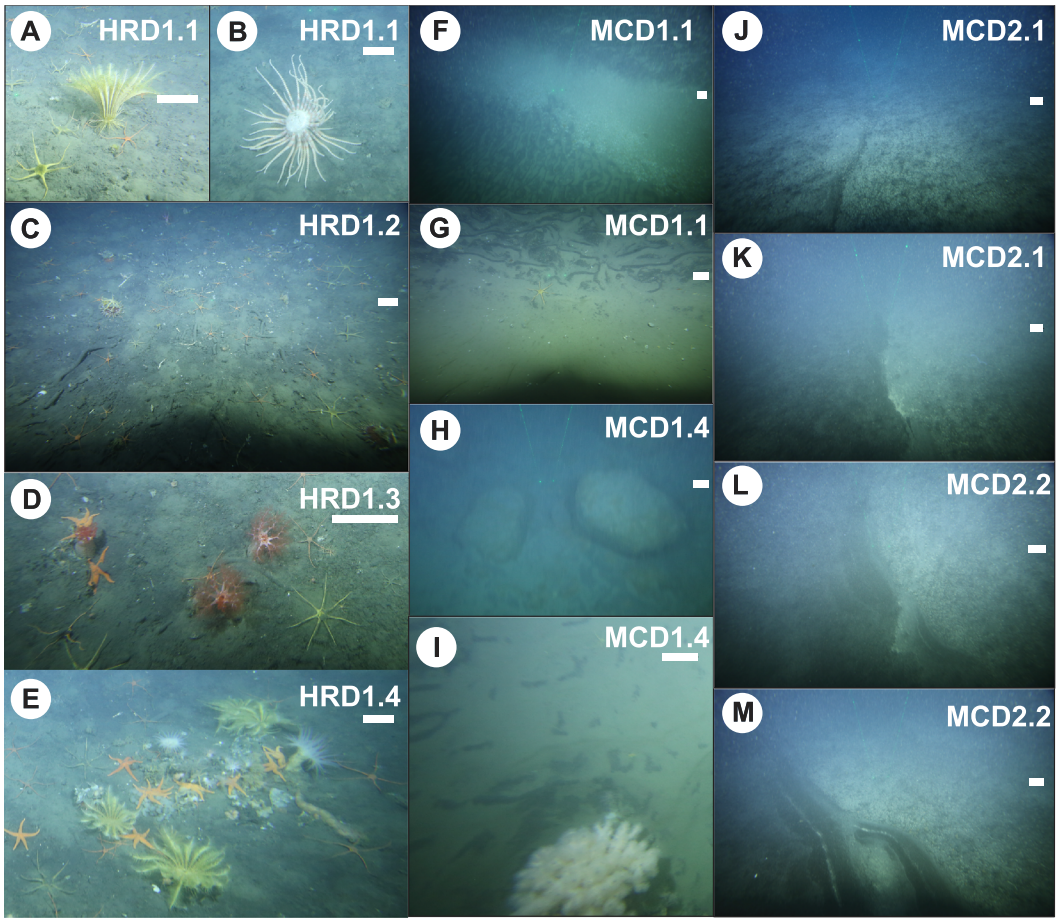

Figure 6. Photographs from HRD1 **(a-e)** show a variety of benthic species; MCD1 **(f-i)** shows disturbed sediment, ripples and limited benthic species; and, MCD2 **(j-m)** show ~20 cm wide and tens of meters long marks on the seafloor, with no benthic species. White scale bars are 10 cm long at the seafloor. Camera tows are shown in Fig. 2.

Twenty-four of 32 water samples near flares show δ^3He exceeding background levels, ranging from 0.29 to 10.09 δ^3He% (Figure 7b). Two values are greater than typical δ^3He values of ~8% from mid-ocean ridge basalts (MORB): 8.22% (CTD-20) and 10.09% (CTD-36), both from CTD casts near MCD1 seeps (MCD1.1 and MCD1.5, respectively; Figures 7b and c). The next highest values, 6.0% (CTD-32), 4.5% (CTD-38), and 3.6% (CTD-39), were also proximal to MCD1. The CTD casts in the nearest HRD1 flares are CTD-51 (~550 m) and CTD-52 (600 m) from the large quadruple flare. CTD-51 had δ^3He% of 1.69; CTD-52 had δ^3He% of 3.27.

3.6. Geochemistry of Seep Sediments

Sediments sampled from both HRD1 grabs (SMG-03 and SMG-05; Figure 2c) are comprised of fine basaltic silty mud, with <2-mm grain sizes (Figure 8a). Despite the similarity of grain sizes, the two HRD grabs exhibit highly different isotopic values. SMG-03 showed the most positive and widest range δ^{34}S values (range 3.5‰ to 19.1‰, mean 10.6‰, n = 14) when compared to the far more negative SMG-08 δ^{34}S values (range −12.0‰ to 9.5‰, mean −2.62‰, n = 6; Figure 8b; Table S4). SMG-03 exhibited more negative $\delta^{13}C_{org}$ values (range −29.9‰ to −24.5‰, mean −27.1‰, n = 14) when compared with SMG-08 $\delta^{13}C_{org}$ values (range −23.9‰ to −16.3‰, mean −21.2‰, n = 6), leading to a smaller fractionation factor between the two carbon phases (~25% compared to >30%; Figure 8b). Carbon isotopic values for carbonate within the sediments were lacking in some samples due to low yield for analysis.

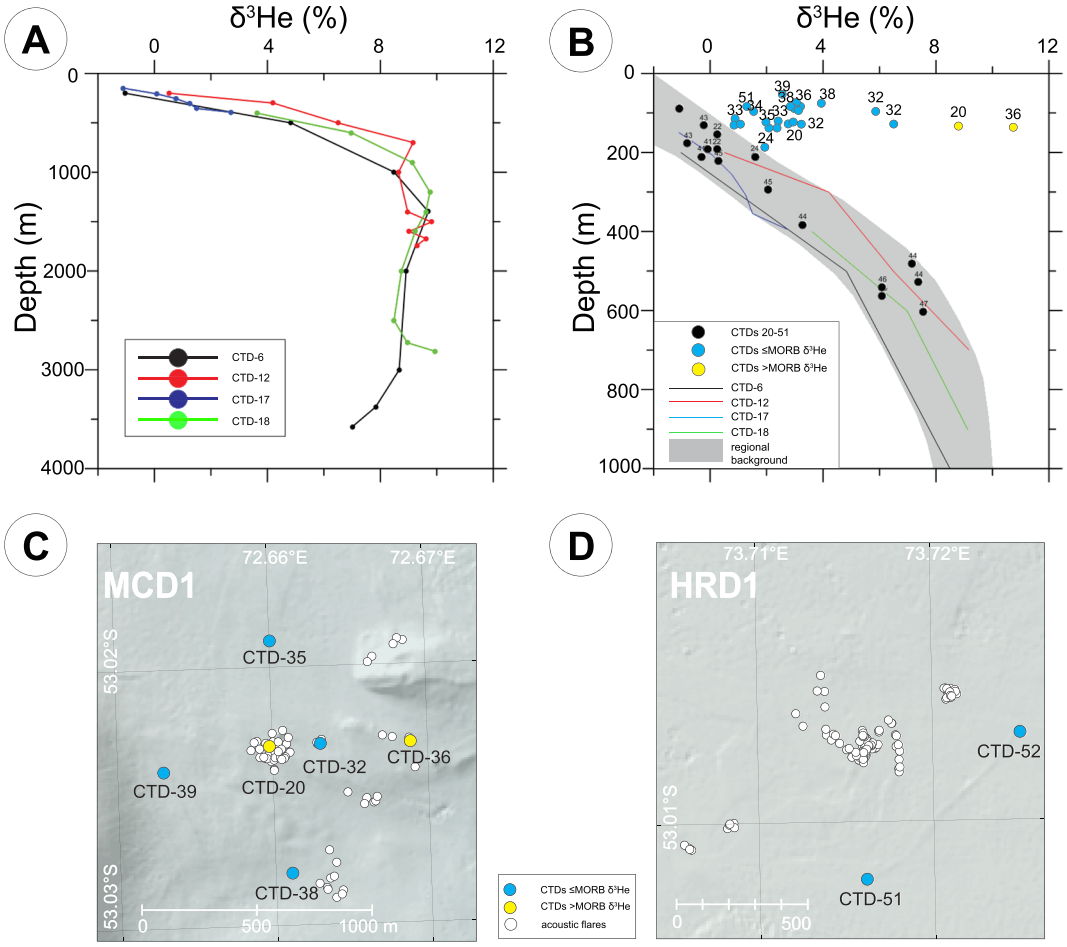

Figure 7. (a) Profiles of background δ^3He versus depth at four locations on the Central Kerguelen Plateau (see Figure 2d). The four profiles are similar to those found throughout the southern Indian Ocean. (b) Plot of δ^3He versus depth for shallow samples collected at flare sites on the flanks of HIMI. Small numbers are the ship CTD casts. Solid lines are δ^3He profiles from the Kerguelen Plateau (Figure 2d and Figure 7a). Shaded area shows regional background based on the Kerguelen Plateau profiles. Several shallow samples show δ^3He in excess of regional background and ≤MORB (blue dots); two samples show δ^3He > MORB (yellow dots), unambiguous evidence for local input of ^{3}He-rich fluid or gas. (c) Map of MCD samples with δ^3He above regional background (blue dots), samples with δ^3He > MORB (yellow dots), and flare bases (white dots). (d) Map of HRD samples with δ^3He above regional background (blue dots) and flare bases (white dots).

4. Discussion

We observed 13 submarine gas seeps near HIMI, the first scientific evidence for submarine gas emission on the ~1.8 x 10^6 km^2 Kerguelen Plateau. The Kerguelen Plateau LIP in the remote southern Indian Ocean has a long sustained history of active subaerial volcanism and glacial/interglacial cycles of sedimentation, both of which make the area a likely candidate for submarine gas emissions. Our multifrequency analysis of the observed hydroacoustic flares confirms gas release near both island groups; this analysis also allowed us to approximate relative bubble sizes of the seeps. In the absence of direct gas samples being obtained from these remote seeps, we examine hydroacoustic, water column, geochemical, geological, and biological indicators to consider the possible mechanism(s) of the HIMI flares.

The shallow (<150 m) marine setting of these sites excludes methane hydrate dissociation, as the necessary high-pressure and low-temperature conditions for hydrate formation are not met (Peckmann et al., 2001). Likewise, liquid CO_2 droplets associated with hydrothermal vents occur beneath the CO_2 phase transition boundary so are thus confined to deeper (>500 m below sea level (MBSL)) sites (Alendal et al., 2013; Konno et al., 2006; Linke et al., 2014; Nakamura et al., 2013). After excluding the above, we explore possible mechanisms for the flares that fit the depth, temperature, and salinity conditions of the two islands:

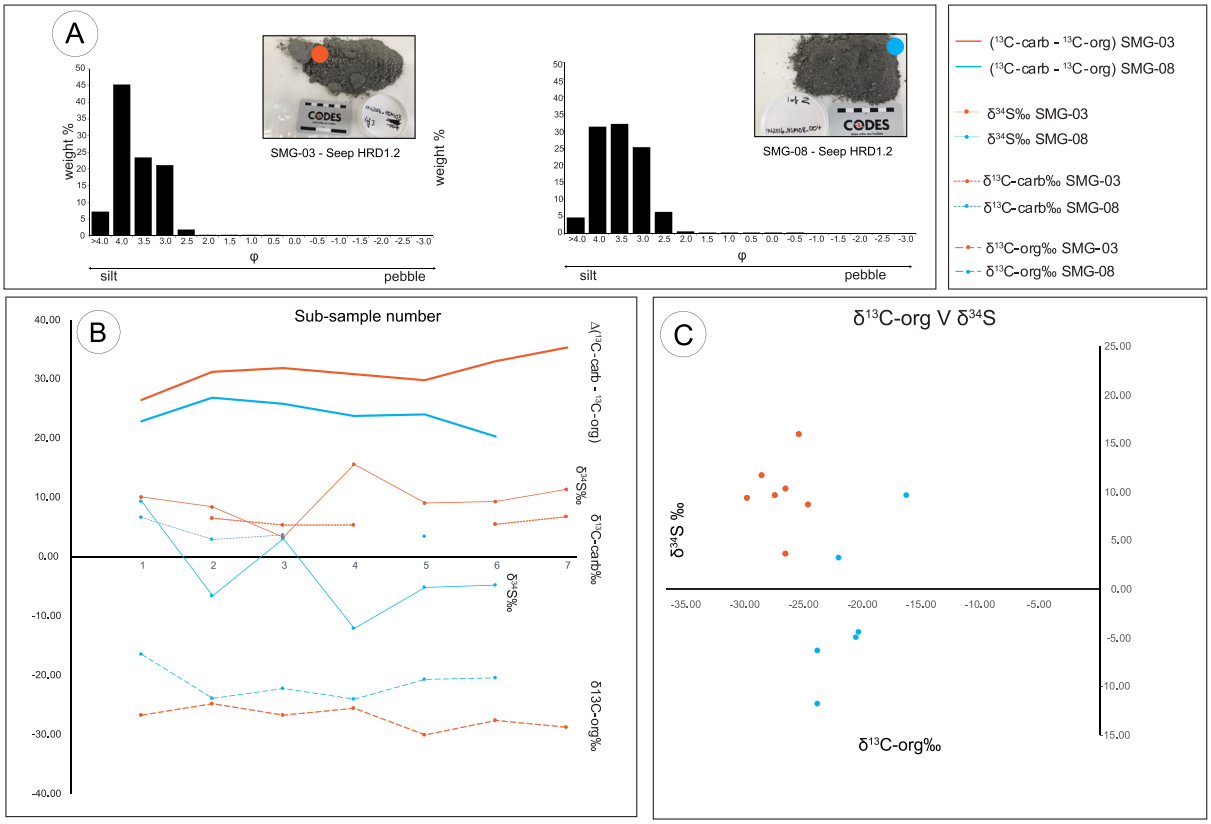

Figure 8. (a) Grain size analysis and photographs showing different seafloor sediments for SMG-03 (orange) and SMG-08 (blue) sites. CODES scale bar, (top) 1-cm increments, and (bottom) 1-in increments. (b) Seven subsample analyses comparison showing discrete values: SMG-03 and SMG-08 for δ^{34}S-CDT‰ (Cañon Diablo Troilite standard), δ^{13}Ccarb-PDB (Pee-Dee Belemnite standard), and δ^{13}Corg-PDB (Pee-Dee Belemnite standard). (c) Plot of δ^{13}Corg‰ versus δ^{34}S‰.

(1) methane bubbles associated with biogenic cold seeps; (2) methane bubbles associated with thermogenic gas release; (3) CO_2, abiotic methane, and other minor gas bubbles associated with shallow diffuse hydrothermalism; or (4) a combination of the three, such as a sediment-hosted geothermal system (Procesi et al., 2019).

At Heard Island (HRD1), the lack of >MORB ^{3}He/^{4}He ratios (expected for hydrothermal venting) may suggest gas release either unrelated to hydrothermal activity or predominantly related to a different gas release mechanism. The helium samples in the nearest HRD1 flares, however, were > 500 m from the largest flare; thus, any potential weak signal may not be captured. Seafloor sediment sulfides formed at MORB hydrothermal systems typically have δ^{34}S values in the narrow range of 0% to +5 ‰, similar to magmatic sulfur (Herzig et al., 1998). The HRD sediment grab samples show two distinctly different ^{34}S values: SMG-03 sediments show positive ^{34}S and negative $^{13}C_{org}$; SMG-08 shows a decoupled carbon and sulfur isotope trend (increasing positive $^{13}C_{org}$ values with much more negative ^{34}S values; Figure 8c) consistent with biogenic sulfide and pyrite formation associated with microbial reduction of marine sulfate in surface sediments, typical for marine sediments (Jørgensen et al., 2004). The combined sulfur isotopic values for both grabs exhibit a much larger range (–12.0‰ to +19.1‰) than those expected from a pure volcanic/hydrothermal source (+0‰ to 5‰), barite formation (+4‰ to 27‰), or water column source (~ + 20‰) (Herzig et al., 1998; Orphan et al., 2004). The negative ^{13}C results from both samples may be explained by the expulsion of thermogenic gas (deep buried organic matter warmed by a shallow heat source) causing a depletion in ^{13}C organic carbon, though we cannot determine if the ^{13}C organic values represent the influence of water column biomass on surface sediments (Lorant et al., 1998; Scott et al., 1994). The combined negative and positive ^{34}S of the two grabs may suggest both strong methane production and weak hydrothermal expulsion, although we cannot determine the source for the positive values (whether hydrothermal sulfur or water column sulfate).

The yellow accumulations observed at HRD1 may either be of the following: (a) dense pigmented bacterial mats or (b) inorganic mineral precipitate. If the accumulations observed are pigmented mats (as opposed to unpigmented or white bacterial mats), similar to yellow-orange *Beggiatoa* mats observed at Hydrate Ridge (Boetius & Suess, 2004; Tryon et al., 2002), these commonly have little to no CO_2 incorporation ability and are considered heterotrophic or methanotrophic, with methane and H_2S instead serving as the energy source for the microbial communities (Nikolaus et al., 2003; Sassen et al., 1998). Alternatively, if the accumulations are instead evidence of mineral precipitation, such as Fe-oxyhydroxides crusts observed but also unsampled at Hook Ridge, Antarctica (Bohrmann et al., 1999; Petersen et al., 2004), a relict or extremely low magnitude hydrothermal source may be suggested. Physical samples of the accumulations would be required to confirm their origin. No high reflective signals in the seafloor bathymetry backscatter (not shown) were observed; high backscatter signals usually indicate slabs of authigenic carbonate and are diagnostic of high-magnitude seeps (Hovland et al., 2012). HRD1 also hosts a flourishing ecosystem of echinoderms, anemones, skates, rays, and fish, with no indication of localized acidification or reduced biodiversity that would typically accompany shallow diffuse hydrothermal venting with associated CO_2 and other minor gas release.

More broadly, offshore conditions around Heard Island are optimal for cold methane seeps: a large supply of sediment from glaciers, relatively sheltered coastal shelf, and an intraplate setting has allowed thick deposits of organic matter to accumulate over time (Hovland et al., 2012; Reeburgh, 2007). The alternating lithologies in the subbottom data at HRD1 suggest strongly reflective volcanogenic material overlain by weakly reflective hemipelagic sediment (see section 3.5). We suggest the acoustic blanking observed beneath HRD1 flares as evidence of shallow gas reservoirs and possible gas conduits, rising from the base of the imaged sediments to the yellow horizon (Figures 4f and 4g). Unlike water and sediment, gas absorbs acoustic energy; thus blanking in subseafloor sediments is commonly interpreted as pooling gas (Davies et al., 1997; Fleischer et al., 2001; Tóth et al., 2014; Tóth et al., 2015). The subsurface acoustic lenses beneath HRD1 (Figures 4f and 4g), and farther northeast of Heard Island, may be related to paleo-glacial conditions, such as meltwater channels and associated eskers formed by subglacial hydrological flow when glaciers extended farther from HIMI onto the Central Kerguelen Plateau.

At the McDonald Islands, elevated ^3He levels (>MORB; Figure 7) observed in the water column suggest some form of a primitive source material nearby (e.g., hydrothermal venting; Craig & Lupton, 1976). High ^3He ratios (>MORB levels of ~8%), as observed in the two samples proximal to MCD1 seeps, provide definitive evidence of deep-mantle input into the water column such as diffuse hydrothermal venting undetectable to our echosounders. Samples with $^3He/^4He$ ratios ≤MORB, however, such as the remaining samples around both islands, are less definitive proof of mantle input (Hilton et al., 1995; Poreda et al., 1992). Hydrothermal fluid venting (or other fluid escape) would not provide sufficient acoustic contrast to form flares; CO_2, abiotic methane, and other minor gas bubbles associated with shallow diffuse hydrothermal venting, however, could provide such a contrast. Shallow hydrothermal vents are unique due to the presence of a gas phase, absent at deep-sea vents (Tarasov et al., 2005), and often have no detectable difference in seawater temperatures as the gases cool rapidly as they rise (Passaro et al., 2014; Passaro et al., 2016). Shallow diffuse hydrothermal gas is usually dominated by CO_2 due to degassing slab or magma, with abiotic CH_4, H_2S, and H_2 also important components (Dando, 2010).

In areas of shallow CO_2 (and other minor gas) venting, reduced biodiversity is expected as localized acidification results in fewer taxa with acidification-tolerant species dominating (Dando, 2010; Hall-Spencer et al., 2008; Kroeker et al., 2011). At MCD1, we observe few to no benthic communities and low biodiversity and at MCD2 a complete absence of visible biota. The gas escape causing the flares we observed might reasonably be expected to be composed of CO_2, H_2S, abiotic CH_4, and other minor gases. Offshore conditions around the McDonald Islands are less amenable to hosting cold methane seeps: the McDonald Islands host no glaciers to deliver large volumes of sediment offshore; the islands also bear the brunt of the eastward flowing Antarctic Circumpolar Current, inhibiting most sediment from accumulating. The subbottom profile across both MCD1 and MCD2 seeps is interpreted as a hard surface covered in a thin layer of reflective volcanogenic sediments (see section 3.5). The thin (<10 m) sediment accumulation observed in the subbottom at MCD1 may host methanogens; however, the flare intensity appears out of proportion to the amount of sediment potentially detected. Sediment accumulation also appears minimal at MCD2, but strong, persistent

flares are still observed indicating a point source of gas release. Without core samples, however, true sediment extent cannot be determined. The presence of acoustically reflective volcanogenic sediment may have inhibited signal penetration, and as such, sediment may be present below the uppermost reflective layer but undetectable with our systems. Seismic data collected northwest of McDonald Islands (Borissova et al., 2002), however, show little to no sedimentation above hard, volcanic basement; low sedimentation rates may, therefore, be common around McDonald Islands.

Based on our observations, we speculate that the Heard Island flares may result from either cold methane seepage or are indicators of a sediment-hosted geothermal system (Procesi et al., 2019). The nearby volcanism of Heard Island, and related geothermal heat, may be enhancing the maturation potential of methanogens or thermally degrading organic matter in the thick seafloor sediments resulting in a possible dual biogenic-thermogenic methane source for seafloor gas at HRD1, alongside volcanic gas emissions, as observed at sediment-hosted geothermal systems (Procesi et al., 2019). The lack of a high ^{3}He excess (>MORB) near Heard Island suggests that the bubbles observed are primarily methanogenic in origin. Two, possibly dual, mechanisms remain: sedimentary biogenic methane from near-surface anoxic sediments or δ^{13}C-enriched methane from thermogenic processes. The presence of possible gas conduits observed as acoustic blanking in deeper sediments (Figures 4e and 4f), the isotopic depletion of ^{13}C organic carbon (Figure 8a), and nearby active volcanism contributing geothermal heat suggest a possible dual biogenic-thermogenic methane source for the gas emissions. The lower ^{3}He ratios (≤MORB) and possible Fe-oxyhydroxide precipitation could suggest a relict or extremely low magnitude hydrothermal venting proximal to, but not a primary cause of, flares.

In contrast, we speculate that the McDonald Islands flares at MCD1 and MCD2 may be locations of diffuse and point-source gas release, respectively, and are related to shallow CO_2, abiotic methane, and other minor gas emissions. As onshore regions of HIMI are volcanically active (Duncan et al., 2016), observable as subaerial gas emissions, submarine volcanic gas emissions are probable, thus providing an alternate gas source to methane gas escape. The high ^{3}He/^{4}He ratios (>MORB) at MCD1 suggest that these flares may result from gas emissions analogous to those observed coincident with hydrothermalism at shallow convergent plate margins or hotspot volcanoes (Ingrassia et al., 2015; Monecke et al., 2012; Passaro et al., 2014; Passaro et al., 2016; Pérez et al., 2014). The scarcity of sediments containing organic matter proximal to the McDonald Islands seeps, and thus the nonviability for sampling, suggests a biogenic source is not primarily responsible for the flares being observed. The McDonald Islands emissions may be linked to either faults or submarine extensions of subaerial geothermal systems, such as those observed subaerially on the islands (McIvor, 2007; Quilty & Wheller, 2000; Stephenson et al., 2005). Active fumaroles were observed degassing on the McDonald Islands during data collection for this study.

4.1. Implications for McDonald Islands Flares

The McDonald Islands seeps may represent one of very few known shallow intraplate gas vents. Though shallow-water hydrothermal venting is common at convergent margins (Passaro et al., 2014; Passaro et al., 2016; Tarasov et al., 2005), few examples of shallow-water venting in intraplate circumstances have been observed globally. Of more than 600 identified submarine gas vents (Beaulieu et al., 2013), 61 (~10%) are found in shallow (<200 m) waters. Of the 61 shallow sites reported by Beaulieu et al. (2013), only 2 are found in intraplate settings. The two examples of shallow intraplate vent sites are within the Azores archipelago in the North Atlantic, associated with the Azores hotspot, and the basaltic McDonald seamount in the South Pacific, associated with the McDonald hotspot. The Azores archipelago hosts nine vents degassing bubbles composed of ~90% CO_2 (Aguiar & Costa, 2010; Couto et al., 2015; Rajasabapathy et al., 2015), including shallow (~35 m depth) low-temperature bubble emissions (Munaro et al., 2010). The McDonald seamount also has extensive shallow gas (methane, CO_2, and SO_4) release observed exiting shallow (156 m) seafloor sediments (Cheminée et al., 1991).

Subsequent to the Beaulieu et al. (2013) review, work on El Hierro Island in the North Atlantic, associated with the Canary hotspot, suggests that it may be another relevant analogue. Evidence for gas venting has been observed in water 88 to 350 m deep around El Hierro (Beaulieu et al., 2013; Pérez et al., 2012; Pérez et al., 2014; Somoza et al., 2017). Flares were recorded along with CO_2 and H_2S degassing and pyroclastic plumes during the 2011–2012 eruption (Pérez et al., 2012; Pérez et al., 2014), with significant discharge of

CO_2 continuing after the eruption (Santana-Casiano et al., 2016). El Hierro, thought to be above the present Canary hotspot location, is composed primarily of alkali picrite and basanite though it hosts some phonolitic lava (Stroncik et al., 2008). The Canary Islands more broadly are largely phonolitic, like the McDonald Islands.

Shallow hydrothermal systems directly affect ecosystem development due to localized acidification and are valuable proxies for how increased ocean acidity may affect benthic communities (Hall-Spencer et al., 2008; Kroeker et al., 2011). Additionally, hydrothermal venting along mid-ocean ridges plays a large part in the ocean energy budget and elemental cycling (Winckler et al., 2010); however, the contribution from shallow-water hydrothermal systems to the global CO_2 budget is, like submarine methane contributions, not well constrained.

4.2. Implications for Heard Island Flares

The Heard Island flares may represent the first cold methane seep observed on the Kerguelen Plateau and the second active methane seep discovered in the Southern Ocean to date (Römer et al., 2014). Unlike most other shallow cold methane seeps (Dupré et al., 2014; Gentz et al., 2014; Römer et al., 2014; Sahling et al., 2014), the water column above the Heard Island seeps has persistent strong vertical mixing (Park et al., 2008) which could remove the usual biological and physical filters, without which methane gas may escape into the atmosphere. Greater depths and the presence of a pycnocline usually inhibit methane escape to the atmosphere (rising bubbles dissolve in the undersaturated water column or are consumed by methanotrophs; Gentz et al., 2014; James et al., 2016). In the presence of a consistent well-mixed water column for HRD1 (Holmes et al., 2019), assuming the flares are dominantly methane and assuming that the gas rises higher than our sounders can observe, we can calculate a maximum estimate of possible methane contribution to the atmosphere. If we assume only ~10% of methane contained in a bubble will reach the surface from depths <100 m (Leifer & Patro, 2002), and assume an average rate of bubble release of one bubble sec^1, with seven discrete bubble release points (three seep groups and a quadruple seep), we estimate ~70 $kg/year^1$ of methane reaching the surface (methane density [3 °C at 90 MBSL] = 7.07 kg/m^3 (Medwin & Clay, 1997); average bubble radius = 5 mm; initial mass of methane per bubble [≥90% methane] = 3.3 x 10^{-6} kg; Leifer & Patro, 2002).

An extensive ice cap covered the Heard Island, possibly the McDonald Islands, and some of the Central Kerguelen Plateau during LGM (Figure 1b; Siddall et al., 2003; Balco, 2007; Hall, 2009; Hodgson et al., 2014). The thick-grounded ice cap conditions favor the formation of methane hydrates. When deglaciation began after LGM, exposed hydrates would begin dissociating if above the GHSZ. All of the reconstructed paleo-ice sheet margin sits at or higher than the ~300-m-deep GHSZ; thus we would expect to find evidence of methane hydrate dissociation over the ~9,600 km^2 inside the paleo-ice sheet margin (Hodgson et al., 2014). If we assume the same density of seeps as HIMI (7 discrete methane seeps in the hydroacoustically observed ~1,278 km^2), as many as 50 additional sites may exist with the potential to contribute >500 $kg/year^1$. While this low flux would not significantly influence the global carbon cycle, for example, in comparison to the East Siberian Arctic Shelf (0.9 Tg/year; Shakhova et al., 2014), the HRD seeps may have localized effects on atmospheric CO_2 drawdown or benthic habitat composition.

5. Conclusions

We observed 13 discrete seeps, observed as flares, at 3 sites proximal to the remote HIMI. This is the first scientific hydroacoustic survey of the region and the first indication of submarine gas emission on the Kerguelen Plateau. Based on hydroacoustic, geophysical, geochemical, and video results, we conjecture the following:

1. Heard Island flares potentially represent a previously unknown cold methane seep of possible combined biogenic and thermogenic origin, originating from thick sediment packages northeast of the island, with nearby onshore volcanism of Heard Island which may be enhancing the maturation potential of sediment-hosted methanogens.
2. McDonald Island flares potentially show evidence of submarine gas emissions associated with unconfirmed shallow diffuse hydrothermal venting, related to active intraplate hotspot volcanism on the island.

The Heard Island seeps may represent the second cold methane seep so far observed in the Southern Ocean. As the methane may not be readily confined within the water column, the Heard Island seeps may contribute a globally negligible, though locally significant, source of methane. If the McDonald Islands seeps represent hydrothermal-related gas venting, our data provide the first evidence of active submarine volcanism on the Kerguelen Plateau. The data expand our limited understanding of the submarine environment of HIMI and add to the limited number of hot vents observed in shallow intraplate settings and on LIPs (Beaulieu et al., 2013).

Our study highlights the value of water column hydroacoustic data for understanding seafloor processes and carbon cycling in the data-poor Southern Ocean and other unmapped or remote regions. Additional seeps may also be present elsewhere within the reconstructed ice sheet margin that covered HIMI and a portion of the Central Kerguelen Plateau during LGM. Extensive sedimentation and other zones of potential submarine volcanic activity on the Kerguelen Plateau means that additional seeps or vents may lie outside the small survey zone proximal to the islands, warranting further study into the nature of gas/fluid exchange on the Kerguelen Plateau and LIPs generally. Future sampling efforts with a remotely operated vehicle to obtain suitable gas tight samples, physical samples of yellow seafloor accumulations, or direct dissolved gas sampling with a towed vehicle or autonomous underwater vehicle would allow us to fully constrain gas composition, bubble release mechanisms, and quantify possible interaction with the atmosphere.

Acknowledgments
We thank the Australian Marine National Facility (MNF) for its support in the form of sea time on RV *Investigator*, support personnel, scientific equipment, and data management. We also thank the captain, crew, and fellow scientists of RV *Investigator* voyage IN2016_V01. We also thank specifically the following: T. Martin, F. Cooke, S. L. Sow, N. Bax, J. Ford, and F. Althaus, CSIRO (Commonwealth Scientific and Industrial Research Organisation); Echoview Software Pty. Ltd. (Hobart, Australia); C. Dietz and C. Cook, Central Science Laboratory, University of Tasmania; C. Wilkinson and T. Baumberger, National Oceanic and Atmospheric Administration; R. Carey, University of Tasmania; T. Holmes, Institute for Marine and Antarctic Studies, University of Tasmania; N. Polmear; and A. Post, Geoscience Australia. The overall science of the project is supported by Australian Antarctic Science Program (AASP) grant 4338. E.S.' PhD research is supported by the Australian Research Council's Special Research Initiative Antarctic Gateway Partnership (Project ID SR140300001) and by an Australian Government Research Training Program Scholarship. S.C.J. is supported by iCRAG under SFI, European Regional Development Fund, and industry partners, as well as ANZIC-IODP. J.M.W. is supported by ARC grant DE140100376 and DP180102280. This is PMEL publication number 4910. All IN2016_V01 data and samples acquired on IN2016_V01 are made publicly available in accordance with MNF policy.

References

Aguiar, P., & Costa, A. C. (2010). Shallow hydrothermal vents and marine protected areas within the Azores archipelago. *Geographic Technologies applied to Marine Spatial Planning and Integrated Coastal Zone Management*.

Alendal, G., Omar, A., Denny, A. R., Baumberger, T., Beaubien, S. E., Veildstädte, L., et al. (2013). Technical synthesis report on droplet/bubble dynamics, plume dynamics and modelling parameters, use of hydro-acoustics to quantify droplet/bubble fluxes, and carbonate system variable assessment. *ECO2 project number: 265847*.

Balco, G. (2007). A surprisingly large marine ice cap at Heard Island during the last glacial maximum? USGS OFR-2007. U.S. Geological Survey and the National Academies.

Beaman, R. J., & O'Brien, P. E. (2011). Kerguelen Plateau bathymetric grid, November 2010. *Geoscience Australia,* Record, 2011/22.

Beaulieu, S. E., Baker, E. T., German, C. R., & Maffei, A. (2013). An authoritative global database for active submarine hydrothermal vent fields. *Geochemistry, Geophysics, Geosystems*, *14*, 4892–4905. https://doi.org/10.1002/2013GC004998

Boetius, A., & Suess, E. (2004). Hydrate ridge: A natural laboratory for the study of microbial life fueled by methane from near-surface gas hydrates. *Chemical Geology*, *205*, 291–310.

Bohrmann, G., Chin, C., Petersen, S., Sahling, H., Schwarz-Schampera, U., Greinert, J., et al. (1999). Hydrothermal activity at Hook Ridge in the Central Bransfield Basin, Antarctica. *Geo-Marine Letters*, *18*, 277–284.

Borissova, I., Moore, A., Sayers, J., Parums, R., Coffin, M. F. & Symonds, P. A. (2002), Geological framework of the Kerguelen Plateau and adjacent ocean basins. *Geoscience Australia,* Record 2002/05.

Brierley, A. S., & Watkins, J. L. (1996). Acoustic targets at South Georgia and the South Orkney Islands during a season on krill scarcity. *Marine Ecology Progress Series*, *138*, 51–61.

Cheminée, J.-L., Stoffers, P., McMurty, G., Richnow, H., Puteanus, D., & Sedwick, P. (1991). Gas-rich submarine exhalations during the 1989 eruption of Macdonald seamount. *Earth and Planetary Science Letters*, *107*, 318–327.

Clift, R., Grace, J. R., & Weber, M. E. (1978). *Bubbles, drops, and particles*. New York: Academic Press.

Coffin, M. F., & Eldholm, O. (1994). Large igneous provinces: crustal structure, dimensions, and external consequences. *Reviews of Geophysics*, *32*, 1–36.

Coffin, M. F., Pringle, M. S., Duncan, R. A., Gladczenko, T. P., Storey, M., Müller, R. D., & Gahagan, L. A. (2002). Kerguelen hotspot magma output since 130 Ma. *Journal of Petrology*, *43*, 1121–1139.

Colbo, K., Ross, T., Brown, C., & Weber, T. (2014). A review of oceanographic applications of water column data from multibeam echosounders. *Estuarine, Coastal and Shelf Science*, *145*, 41–56.

Couto, R. P., Rodrigues, A. S., & Neto, A. I. (2015). Shallow-water hydrothermal vents in the Azores (Portugal). *Revista de Gestão Costeira Integrada*, *15*, 495–505.

Craig, H., & Lupton, J. E. (1976). Primordial neon, helium and hydrogen in oceanic basalts. *Earth and Planetary Science Letters*, *31*, 369–385.

Crawford, A. M., & Hay, A. E. (1993). Determining suspended sand size and concentration from multifrequency acoustic backscatter. *The Journal of the Acoustical Society of America*, *94*.

Dando, P. R. (2010). Biological communities at marine shallow-water vent and seep sites. In "The vent and seep biota - from microbes to ecosystems". Topics in Geomicrobiolgy (Chap. 11, pp. 333–378). Dordrecht: Springer.

Davies, T., Bell, T., Cooper, A., Josenhans, H., Polyak, L., Solheim, A., et al. (1997). *Glaciated continental margins: an atlas of acoustic images*. London: Chapman & Hall.

De Beukelaer, S. M., MacDonald, I. R., Guinnasso, N. L., & Murray, J. A. (2003). Distinct side-scan sonar, RADARSAT SAR, and acoustic profiler signatures of gas and oil seeps on the Gulf of Mexico slope. *Geo-Marine Letters*, *23*, 177–186.

Duncan, R. A., Quilty, P., Barling, J., & Fox, J. (2016). Geological development of Heard Island, Central Kerguelen Plateau. *Australian Journal of Earth Sciences*, *63*, 81–89.

Dupré, S., Berger, L., Le Bouffant, N., Scalabrin, C., & Bourillet, J.-F. (2014). Fluid emissions at the Aquitaine Shelf (Bay of Biscay, France): A biogenic origin or the expression of hydrocarbon leakage? *Continental Shelf Research*, *88*, 24–33.

Durand, A., Chase, Z., Noble, T. L., Bostock, H., Jaccard, S. L., Kitchener, P., et al. (2017). Export production in the New Zealand region since the last glacial maximum. *Earth and Planetary Science Letters*, *469*, 110–122. https://doi.org/10.1016/j.epsl.2017.03.035

Everson, I., Goss, C., & Murray, W. A. (1993). Comparison of krill (Euphasia superba) density estimated using 38 and 120 kHz echo-sounders. *Marine Biology*, *116*, 269–275.
Fleischer, P., Orsi, T., Richardson, M., & Anderson, A. (2001). Distribution of free gas in marine sediments: a global overview. *Geo-Marine Letters*, *21*, 103–122.
Foote, K. G., Knudsen, H., Vestnes, G., MacLennan, D. N., & Simmonds, E. J. (1987). Calibration of acoustic instruments for fish density estimation: a practical guide. *ICES Cooperative Research report,* 144.
Gentz, T., Damm, E., Schneider von Deimling, J., Mau, S., McGinnis, D. F., & Schlüter, M. (2014). A water column study of methane around gas flares located at the west Spitsbergen continental margin. *Continental Shelf Research*, *72*, 107–118.
Greinert, J., & Nützel, B. (2004). Hydroacoustic experiments to establish a method for the determination of methane bubble fluxes at cold seeps. *Geo-Marine Letters*, *24*, 75–85.
Hall, B. L. (2009). Holocene glacial history of Antarctica and the sub-Antarctic islands. *Quaternary Science Reviews*, *28*, 2213–2230.
Hall-Spencer, J. M., Rodolfo-Metalpa, R., Martin, S., Ransome, E., Fine, M., Turner, S. M., et al. (2008). Volcanic carbon dioxide vents show ecosystem effects of ocean acidification. *Nature*, *454*(7200), 96–99. https://doi.org/10.1038/nature07051
Hay, A. E. (1984). Remote acoustic imaging of the plume from a submarine spring in an arctic fjord. *Science*, *225*, 1154–1157.
Hernández, P. A., Melián, G. V., Somoza, L., Arpa, M. C., Pérez, N. M., Bariso, E., et al. (2017). The acid crater lake of Taal Volcano, Philippines: Hydrogeochemical and hydroacoustic data related to the 2010–2011 volcanic unrest. *Geological Society, London, Special Publications*, *437*(1), 131–152. https://doi.org/10.1144/SP437.17
Herzig, P., Hannington, M. D., & Arribas, A. (1998). Sulfur isotopic composition of hydrothermal precipitates from the Lau back-arc: Implications for magmatic contributions to seafloor hydrothermal systems. *Mineralium Deposita*, *33*, 226–237.
Hilton, D. R., Barling, J., & Wheller, G. E. (1995). Effect of shallow-level contamination on the helium isotope systematics of ocean-island lavas. *Nature*, *373*, 330–333.
Hodgson, D. A., Graham, A. G. C., Roberts, S. J., Bentley, M. J., Cofaigh, C. O., Verleyen, E., et al. (2014). Terrestrial and submarine evidence for the extent and timing of the last glacial maximum and the onset of deglaciation on the maritime-Antarctic and sub-Antarctic islands. *Quaternary Science Reviews*, *100*, 137–158. https://doi.org/10.1016/j.quascirev.2013.12.001
Holmes, T. M., Wuttig, K., Chase, Z., van der Merwe, P., Townsend, A. T., Schallenberg, C., et al. (2019). Iron availability influences nutrient drawdown in the Heard and McDonald Islands region, Southern Ocean. *Marine Chemistry*, *211*, 1–14. https://doi.org/10.1016/j.marchem.2019.03.002
Hovland, M., Jensen, S., & Fichler, C. (2012). Methane and minor oil macro-seep systems—their complexity and environmental significance. *Marine Geology*, *332-334*, 163–173.
Ingrassia, M., Martorelli, E., Bosman, A., Macelloni, L., Sposato, A., & Chiocci, F. L. (2015). The Zannone giant pockmark: First evidence of a giant complex seeping structure in shallow-water, central Mediterranean Sea, Italy. *Marine Geology*, *363*, 38–51.
James, R. H., Bousquet, P., Bussmann, I., Haeckel, M., Kipfer, R., Leifer, I., et al. (2016). Effects of climate change on methane emissions from seafloor sediments in the Arctic Ocean: A review. *Limnology and Oceanography*, *61*(S1), S283–S299. https://doi.org/10.1002/lno.10307
Johnson, S. C., Large, R. R., Coveney, R. M., Kelley, K. D., Slack, J. F., Steadman, J. A., et al. (2017). Secular distribution of highly metalliferous black shales corresponds with peaks in past atmosphere oxygenation. *Mineralium Deposita*, *52*, 791–798.
Jørgensen, B. B., Böttcher, M. E., Lüschen, H., Neretin, L. N., & Volkov, I. I. (2004). Anaerobic methane oxidation and a deep H 2 S sink generate isotopically heavy sulfides in Black Sea sediments. *Geochimica et Cosmochimica Acta*, *68*, 2095–2118.
Judd, A. G. (2003). The global importance and context of methane escape from the seabed. *Geo-Marine Letters*, *23*, 147–154.
Judd, A. G., & Hovland, M. (2009). *Seabed fluid flow: The impact on geology, biology and the marine environment*. Cambridge: Cambridge University Press.
Kirschke, S., Bousquet, P., Ciais, P., Saunois, M., Canadell, J. G., Dlugokencky, E. J., et al. (2013). Three decades of global methane sources and sinks. *Nature Geoscience*, *6*(10), 813–823. https://doi.org/10.1038/ngeo1955
Konno, U., Tsunogai, U., Nakagawa, F., Nakaseama, M., Ishibashi, J.-I., Nunoura, T., & Nakamura, K.-I. (2006). Liquid CO2 venting on the seafloor: Yonaguni Knoll IV hydrothermal system, Okinawa Trough. *Geophysical Research Letters*, *33*, L16607. https://doi.org/10.1029/2006GL026115
Kroeker, K. J., Micheli, F., Gambi, M. C., & Martz, T. R. (2011). Divergent ecosystem responses within a benthic marine community to ocean acidification. *Proceedings of the National Academy of Sciences*, *108*, 14,515–14,520.
Leifer, I., & Patro, R. K. (2002). The bubble mechanism for methane transport from the shallow sea bed to the surface: a review and sensitivity study. *Continental Shelf Research*, *22*, 2409–2428.
Linke, P., Haeckel, M., Schneider von Deimling, J., Vielstädte, L., Schmidt, M., Sommer, S., et al. (2014). Fluxes of CO2 from natural seep sites and Sleipner storage site. GEOMAR.
Lorant, F., Prinzhofer, A., Behar, F., & Huc, A. Y. (1998). Carbon isotopic and molecular constraints on the formation and the expulsion of thermogenic hydrocarbon gases. *Chemical Geology*, *147*, 249–264.
Madureira, L. S. P., Everson, I., & Murphy, E. J. (1993). Interpretation of acoustic data at two frequencies to discriminate between Antarctic krill (Euphausia superba Dana) and other scatterers. *Journal of Plankton Research*, *15*, 787–802.
McCartney, B. S., & Bary, B. M. (1965). Echo-sounding on probable gas bubbles from the bottom of Saanich Inlet, British Columbia. *Deep Sea Research*, *12*, 285–294.
McGinnis, D. F., Greinert, J., Artemov, Y., Beaubien, S. E., & Wüest, A. (2006). Fate of rising methane bubbles in stratified waters: How much methane reaches the atmosphere? *Journal of Geophysical Research*, *111*, C09007. https://doi.org/10.1029/2005JC003183
McIvor, E. (2007). Heard Island and McDonald Islands. *Papers and Proceedings of the Royal Society of Tasmania*, *141*, 7–10.
Medwin, H., & Clay, C. S. (1997). *Fundamentals of acoustical oceanography*. San Diego, CA: Academic Press.
Monecke, T., Petersen, S., Hannington, M. D., Anzidei, M., Esposito, A., Giordano, G., et al. (2012). Explosion craters associated with shallow submarine gas venting off Panarea island, Italy. *Bulletin of Volcanology*, *74*(9), 1937–1944. https://doi.org/10.1007/s00445-012-0651-8
Munaro, M., Boccolato, G., Ferreira, F., Gracias, N., Sebastião, L., Sotiropolous, P., et al. (2010). Azores FREEsubNET workshop: Habitat mapping of Espalamaca vents and Monte da Guia. *Final FREEsubNET Workshop Report*.
Murton, B. J., Klinkhammer, G., Becker, K., Briasis, A., Edge, D., Hayward, N., et al. (1994). Direct evidence for the distribution and occurence of hydrothermal activity between 27°N–30°N on the mid-Atlantic ridge. *Earth and Planetary Science Letters*, *124*, 119–128.
Nakamura, K., Kawagucci, S., Kitada, K., Kumagai, H., Takai, K., & Okino, K. (2015). Water column imaging with multibeam echo-sounding in the mid-Okinawa trough: Implications for distribution of deep-sea hydrothermal vent sites and the cause of acoustic water column anomaly. *Geochemical Journal*, *49*, 579–596.

Nakamura, K., Toki, T., Mochizuki, N., Asada, M., Ishibashi, J., Nogi, Y., et al. (2013). Discovery of a new hydrothermal vent based on an underwater, high-resolution geophysical survey. *Deep Sea Research, Part I*, *74*, 1–10. https://doi.org/10.1016/j.dsr.2012.12.003

Nikolaus, R., Ammerman, J. W., & MacDonald, I. R. (2003). Distinct pigmentation and trophic modes in Beggiatoa from hydrocarbon seeps in the Gulf of Mexico. *Aquatic Microbial Ecology*, *32*, 85–93.

Orphan, V. J., Ussler, W., Naehr, T. H., House, C. H., Hinrichs, K. U., & Paull, C. K. (2004). Geological, geochemical, and microbiological heterogeneity of the seafloor around methane vents in the Eel River Basin, offshore California. *Chemical Geology*, *205*, 265–289.

Park, Y.-H., Fuda, J.-L., Durand, I., & Naveira Garabato, A. C. (2008). Internal tides and vertical mixing over the Kerguelen Plateau. *Deep Sea Research Part II: Topical Studies in Oceanography*, *55*, 582–593.

Passaro, S., Genovese, S., Sacchi, M., Barra, M., Rumolo, P., Tamburrino, S., et al. (2014). First hydroacoustic evidence of marine, active fluid vents in the Naples Bay continental shelf (southern Italy). *Journal of Volcanology and Geothermal Research*, *285*, 29–35. https://doi.org/10.1016/j.jvolgeores.2014.08.001

Passaro, S., Tamburrino, S., Vallefuoco, M., Tassi, F., Vaselli, O., Giannini, L., et al. (2016). Seafloor doming driven by degassing processes unveils sprouting volcanism in coastal areas. *Scientific Reports*, *6*(1), 22448. https://doi.org/10.1038/srep22448

Peckmann, J., Reimer, A., Luth, U., Luth, C., Hansen, B. T., Heinicke, C., et al. (2001). Methane-derived carbonates and authigenic pyrite from the northwestern Black Sea. *Marine Geology*, *177*, 129–150.

Pérez, N. M., Padilla, G. D., Padrón, E., Hernández, P. A., Melián, G. V., Barrancos, J., et al. (2012). Precursory diffuse CO2 and H2S emission signatures of the 2011–2012 El Hierro submarine eruption, Canary Islands. *Geophysical Research Letters*, *39*, L16311. https://doi.org/10.1029/2012GL052410

Pérez, N. M., Somoza, L., Hernández, P. A., de Vallejo, L. G., León, R., Sagiya, T., et al. (2014). Evidence from acoustic imaging for submarine volcanic activity in 2012 off the west coast of El Hierro (Canary Islands, Spain). *Bulletin of Volcanology*, *76*(12), 882. https://doi.org/10.1007/s00445-014-0882-y

Petersen, S., Herzig, P. M., Schwarz-Schampera, U., Hannington, M. D., & Jonassona, I. R. (2004). Hydrothermal precipitates associated with bimodal volcanism in the Central Bransfield Strait, Antarctica. *Mineralium Deposita*, *39*, 358–379.

Poreda, R. J., Craig, H., Arnórsson, S., & Welhan, J. A. (1992). Helium isotopes in Icelandic geothermal systems: I. 3He, gas chemistry, and 13C relations. *Geochimica et Cosmochimica Acta*, *56*, 4221–4228.

Procesi, M., Ciotoli, G., Mazzini, A., & Etiope, G. (2019). Sediment-hosted geothermal systems: Review and first global mapping. *Earth-Science Reviews*, *192*, 529–544. https://doi.org/10.1016/j.earscirev.2019.03.020

Quilty, P., & Wheller, G. (2000). Heard Island and the McDonald Islands: A window into the Kerguelen Plateau. *Papers and Proceedings of the Royal Society of Tasmania*, *133*, 1–12.

Rajasabapathy, R., Mohandass, C., Yoon, J. H., Dastager, S. G., Liu, Q., Khieu, T. N., et al. (2015). Vitellibacter nionensis sp. nov., isolated from a shallow water hydrothermal vent. *International Journal of Systematic and Evolutionary Microbiology*, *65*(Pt 2), 692–697. https://doi.org/10.1099/ijs.0.070805-0

Reeburgh, W. S. (2007). Oceanic methane biogeochemistry. *Chemical Reviews*, *107*, 486–513.

Riedel, C., Schmidt, M., Botz, R., & Theilen, F. (2001). The Grimsey hydrothermal field offshore north Iceland: Crustal structure, faulting and related gas venting. *Earth and Planetary Science Letters*, *193*, 409–421.

Römer, M., Torres, M., Kasten, S., Kuhn, G., Graham, A. G. C., Mau, S., et al. (2014). First evidence of widespread active methane seepage in the Southern Ocean, off the sub-Antarctic island of South Georgia. *Earth and Planetary Science Letters*, *403*, 166–177. https://doi.org/10.1016/j.epsl.2014.06.036

Rona, P. A., Jackson, D. R., Bemis, K. G., Jones, C. D., Mitsuzawa, K., Palmer, D. R., & Silver, D. (2002). Acoustics advances study of sea floor hydrothermal flow. *Eos, Transactions American Geophysical Union*, *83*, 497–502.

Rona, P. A., Palmer, D. R., Jones, C., Chayes, D. A., Czarnecki, M., Carey, E. W., & Guerrero, J. C. (1991). Acoustic imaging of hydrothermal plumes, East Pacific Rise, 21øN, 109øW. *Geophysical Research Letters*, *18*, 2233–2236.

Sahling, H., Römer, M., Pape, T., Bergès, B., dos Santos Fereirra, C., Boelmann, J., et al. (2014). Gas emissions at the continental margin west of Svalbard: mapping, sampling, and quantification. *Biogeosciences*, *11*(21), 6029–6046. https://doi.org/10.5194/bg-11-6029-2014

Santana-Casiano, J. M., Fraile-Nuez, E., Gonzalez-Davila, M., Baker, E. T., Resing, J. A., & Walker, S. L. (2016). Significant discharge of CO2 from hydrothermalism associated with the submarine volcano of El Hierro Island. *Scientific Reports*, *6*, 25686.

Sassen, R., MacDonald, I. R., Guinnasso, N. L., Joye, S. B., Requejo, A. G., Sweet, S. T., et al. (1998). Bacterial methane oxidation in sea-floor gas hydrate: Significance to life in extreme environments. *Geology*, *26*(9), 851–854. https://doi.org/10.1130/0091-7613(1998)026<0851:BMOISF>2.3.CO;2

Scott, A. R., Kaiser, W. R., & Ayers, W. B. Jr. (1994). Thermogenic and secondary biogenic gases, San Juan Basin, Colorado, and New Mexico—implications for coalbed gas producibility. *AAPG Bulletin*, *78*, 1186–1209.

Shakhova, N., Semiletov, I., Leifer, I., Sergienko, V., Salyuk, A., Kosmach, D., et al. (2014). Ebulition and storm-induced methane release from the East Siberian Arctic Shelf. *Nature Geoscience*, *7*(1), 64–70. https://doi.org/10.1038/ngeo2007

Siddall, M., Rohling, E. J., Almogi-Labin, A., Hemleben, C., Meischner, D., Schmelzer, I., & Smeed, D. A. (2003). Sea-level fluctuations during the last glacial cycle. *Nature*, *423*, 853–858.

Somoza, L., González, F. J., Barker, S. J., Madureira, P., Medialdea, T., de Ignacio, C., et al. (2017). Evolution of submarine eruptive activity during the 2011–2012 El Hierro event as documented by hydroacoustic images and remotely operated vehicle observations. *Geochemistry, Geophysics, Geosystems*, *18*, 3109–3137. https://doi.org/10.1002/2016GC006733

Stephenson, J. O. N., Budd, G. M., Manning, J., & Hansbro, P. (2005). Major eruption-induced changes to the McDonald Islands, southern Indian Ocean. *Antarctic Science*, *17*, 259–266.

Stroncik, N. A., Klügel, A., & Hansteen, T. H. (2008). The magmatic plumbing system beneath El Hierro (Canary Islands): Constraints from phenocrysts and naturally quenched basaltic glasses in submarine rocks. *Contributions to Mineralogy and Petrology*, *157*, 593–607.

Suess, E. (2014). Marine cold seeps and their manifestations: Geological control, biogeochemical criteria and environmental conditions. *International Journal of Earth Sciences*, *103*, 1889–1916.

Tarasov, V. G., Gebruk, A. V., Mironov, A. N., & Moskalev, L. I. (2005). Deep-sea and shallow-water hydrothermal vent communities: Two different phenomena? *Chemical Geology*, *224*, 5–39.

Tóth, Z., Spiess, V., & Jensen, J. (2014). Seismo-acoustic signatures of shallow free gas in the Bornholm Basin, Baltic Sea. *Continental Shelf Research*, *88*, 228–239.

Tóth, Z., Spiess, V., & Keil, H. (2015). Frequency dependence in seismoacoustic imaging of shallow free gas due to gas bubble resonance. *Journal of Geophysical Research: Solid Earth*, *120*, 8056–8072. https://doi.org/10.1002/2015JB012523

Tryon, M., Brown, K. M., & Torres, M. E. (2002). Fluid and chemical flux in and out of sediments hosting methane hydrate deposits on Hydrate Ridge, OR, II: Hydrological processes. *Earth and Planetary Science Letters*, *201*, 541–557.

Veloso, M., Greinert, J., Mienert, J., & De Batist, M. (2015). A new methodology for quantifying bubble flow rates in deep water using splitbeam echosounders: Examples from the Arctic offshore NW-Svalbard. *Limnology and Oceanography: Methods*, *13*, 267–287.

Weber, T. C., Mayer, L., Jerram, K., Beaudoin, J., Rzhanov, Y., & Lovalvo, D. (2014). Acoustic estimates of methane gas flux from the seabed in a 6000 km2region in the Northern Gulf of Mexico. *Geochemistry, Geophysics, Geosystems*, *15*, 1911–1925. https://doi.org/10.1002/2014GC005271

Weis, D., Frey, F., Schlich, R., Schaming, M., Montigny, R., Damesceno, D., et al. (2002). Trace of the Kerguelen mantle plume: Evidence from seamounts between the Kerguelen Archipelago and Heard Island, Indian Ocean. *Geochemistry, Geophysics, Geosystems*, *3*(6), 1033. https://doi.org/10.1029/2001GC000251

Winckler, G., Newton, R., Schlosser, P., & Crone, T. J. (2010). Mantle helium reveals Southern Ocean hydrothermal venting. *Geophysical Research Letters*, *37*, L05601. https://doi.org/10.1029/2009GL042093

Young, C., & Lupton, J. E. (1983). An ultratight fluid sampling system using cold-welded copper tubing. *Eos, Transactions American Geophysical Union*, *64*.